LLNL-JRNL-833198

Understanding and controlling capsule symmetry in near vacuum hohlraums at the National Ignition Facility

D. P. Higginson, D. J. Strozzi, D. Bailey, S. A. MacLarent, N. B. Meezan, S. C. Wilks, G. Zimmerman

March 28, 2022

Physics of Plasmas

Understanding and controlling capsule symmetry in near vacuum hohlraums at the National Ignition Facility

Drew P. Higginson, D. J. Strozzi, D. Bailey, S. A. MacLaren, N. B. Meezan, S. C. Wilks, and G. Zimmerman
Lawrence Livermore National Laboratory, Livermore, California 94551, USA

(Dated: 25 July 2022)

The near vacuum hohlraum platform is an inertial confinement fusion design on the National Ignition Facility (NIF) that uses the lowest practical density of helium gas of 30 μg/cc to fill the hohlraum; 10 times lower than now used routinely. This has several advantages, such as high laser coupling; however, the inability to understand and simulate the symmetry of the imploded capsule has limited the use of this platform. This work presents the first simulations that are able to accurately capture the highly prolate implosion seen experimentally without unphysical, *ad hoc* model changes. While previous investigations attributed this asymmetry to multi-species interpenetration in the hohlraum, we find this alone has little effect on symmetry. Instead, it is the presence of crossed-beam energy transfer (CBET), occurring with no applied wavelength shift between the laser beams, that increases the laser power to the inner cones and causes a more prolate implosion. The effect of CBET is increased in the simulation model when the hohlraum laser entrance hole (LEH) hardware is included. Using this understanding, CBET is exploited by shifting the inner-beam wavelength by -0.75 Å (at 1ω) with respect to the outer-beams. This transfers laser power to the outer-beams, in contrast to positive wavelength shifts, as done routinely on NIF, and produces a round capsule implosion in our simulations. This work shows the possibility of the near vacuum hohlraum as a viable experimental platform. LLNL-JRNL-833198

I. INTRODUCTION

Indirect drive, inertial confinement fusion (ICF) experiments utilize x-ray radiation to implode millimeter-scale spherical capsules filled with deuterium-tritium (D-T) fuel[37–40]. The ultimate goal of these experiments is to compress and heat the fuel to fusion conditions, so that more energy is generated by fusion reactions than was input into the system[41]. A critical requirement for achieving fusion conditions is a symmetrical implosion of the capsule. The National Ignition Facility (NIF)[42] generates the x-ray radiation drive by directing 192 frequency-tripled laser beams (351 nm at 3ω) into a gas-filled cylinder (hohlraum) with laser entrance holes (LEHs) at each end. As shown in Fig. 1, the NIF laser beams are grouped into inner and outer "cones". The inner cones are directed into the hohlraum at angles of either 23.5° or 30° and act to drive x-ray power onto the waist of the capsule. The outer cones are at either 44.5° or 50° and drive x-ray power onto the capsule poles.

The success of ICF relies, among other things, on the ability to efficiently couple laser energy into x-ray radiation to drive the capsule implosion, and to understand and manipulate the laser drive to create a symmetric capsule implosion. A major factor in meeting these requirements is the amount of helium gas-fill in the hohlraum. Low gas fills, defined here as < 600 μg/cc, have been shown to increase the coupling of laser energy into x-rays by decreasing the laser backscatter caused by stimulated Raman scattering (SRS) and stimulated Brillouin scattering (SBS)[43–48]. This work has also shown that these low fills reduce the amount of suprathermal electrons generated via laser-plasma interactions (LPI).

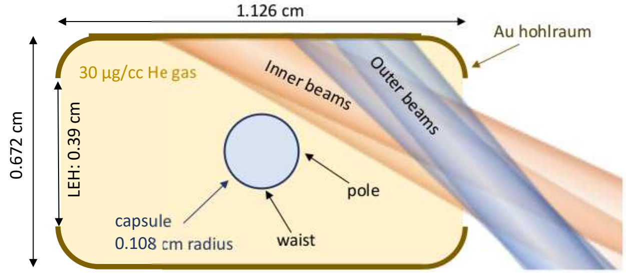

FIG. 1. Simplified schematic of the hohlraum on shot N140702-001. The inner (23.5°, 30°) and outer (44°, 50°) laser cones are shown in one quadrant for simplicity, in practice the lasers come from both sides of the hohlraum and are arranged to cover the azimuthal direction.

However, at the lowest achievable fill density of 30 μg/cc, known as the near vacuum hohlraum (NVH), x-ray symmetry and thus capsule implosion symmetry has not been captured using conventional radiation-hydrodynamic codes[43]. Given that these codes are a fundamental part of the experimental design process, the present practice is to use higher than NVH fill densities, ~ 300 μg/cc, in order to move to a regime where the codes are capable of matching data[47]. While this is a very practical design choice, it means that there exists a region of design space that is avoided simply due to the inability to model low density fills.

Previous work[43,49] postulated that the reason for this discrepancy could be due to the inability of conventional single-fluid, radiation-hydrodynamic codes to model interpenetration between plasma flows. In single fluid simulations, the inner beams appear to be blocked by a high density "ridge" created at the interface between the ablated gold, the helium gas fill and the ablated capsule shell plasmas. The interpenetration hypothesis suggests that this ridge is fictitious, or at least, that it is exaggerated by the fact that in a single-fluid code the plasmas cannot interpenetrate. This hypothesis is supported experimentally under similar laser irradiation conditions on the OMEGA laser showing that gold and carbon are found to interpenetrate in a case with no helium fill[49]. Similar tests were performed using hybrid particle-in-cell simulations[50]. In this experiment, a helium density of 150 μg/cc was found to impede interpenetration, however, a 30 μg/cc fill was not investigated.

In this Article, we investigate the cause of the symmetry discrepancy between single-fluid simulations and experimental data in near vacuum hohlraums. This is done by utilizing the recently implemented multi-species package and the inline crossed-beam energy transfer package[51] in the radiation-hydrodynamic code LASNEX[52,53]. Finally, we use this knowledge to manipulate the implosion symmetry by applying a wavelength shift between the inner and outer beams. We find that a modest shift of -0.75 Å produces a symmetric capsule implosion.

II. EXPERIMENTAL SETUP AND RESULTS

This work focuses on the NIF shot N140702-001, which was previously discussed in Ref.[43]. As shown in Fig. 1, this shot used a 672-scale hohlraum: the inner radius was 0.672 cm, the length was 1.126 cm, and the laser entrance hole (LEH) diameter was 0.394 cm. This was a near vacuum hohlraum (NVH) meaning that the ^{4}He fill inside the hohlraum was 32 μg/cc. The capsule used an undoped, high-density carbon (HDC) ablator, filled with 30%at D and 70%at ^{3}He gas (no ice layer). The laser power profile used in the experiment is shown in Fig. 2; the peak total laser power was 416 TW. This experiment was a 2D convergent ablator (2DConA) experiment, which used two outer laser quads to drive a backlighter foil and make x-ray radiographs of the capsule as it implodes. This introduced some azimuthal asymmetry, which our axisymmetric simulations neglect.

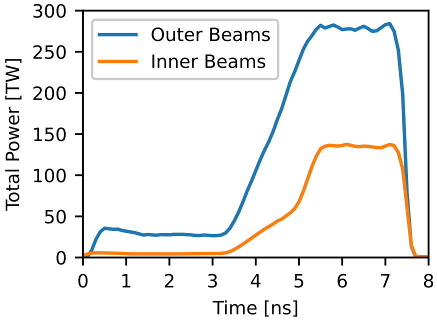

FIG. 2. Measured laser power profiles of the inner and outer beams. The total peak power was 416 TW. Peak power of the inner and outer beams was 136 and 281 TW, respectively.

In order to understand the symmetry of the imploded capsule, a critical component to performance, the self-emitted equatorial x-ray radiation of the capsule was imaged, as shown in Fig. 3. This data is fit with a contour where the emission is 17% of the peak, which is then decomposed into Legendre moments, P_N. The P_0 moment from this data was found to be 62.3 μm, and P_2/P_0 was found to be +56.4%. The positive P_2/P_0 moment indicates that the implosion was prolate ("sausage") and implies that the radiation drive coming from the waist of the hohlraum, where the inner beams are directed was the strongest. In previous work[43], it was not possible for this P_2 asymmetry to be captured using the code HYDRA[54] in its conventional configuration. The authors of this work noticed that a high density "ridge" of material developed at the interface between the gold expansion, the helium fill, and carbon ablator material. This high density region in the simulation caused the inner beams to lose energy in the plasma prior to reaching the waist of the hohlraum, thus creating an x-ray drive leading to a highly oblate ("pancake") capsule implosion. Due to the high relative velocity $\sim$ 500 km/s of the plasma flows, this work[43] hypothesized that the ridge was an artifact of the single-fluid approximation used in the simulation, which excludes the possibility of interpenetration of the flows. Thus, the authors numerically increased the laser frequency from 3ω to 5ω (or higher) in the simulation. This *ad hoc* change increased the critical density for laser propagation without affecting other physics in the simulation, allowing the laser to pass through the ridge and deposit more energy at the waist of the hohlraum. This method increased the P_2 moment of the capsule to create a prolate capsule implosion consistent with experimental data. While this argument seemed logical and convincing at the time, it was not yet possible to test the hypothesis owing to the lack of inclusion of multi-fluid physics in the code.

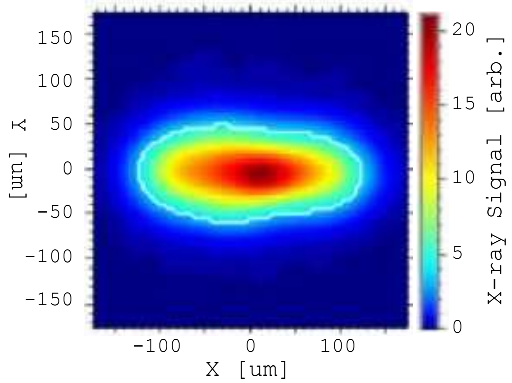

FIG. 3. Experimental time-integrated, equatorial x-ray self emission from shot N140702-001 showing a strongly prolate implosion. The white contour is where the intensity is 17% of the peak. When this contour is fit with Legendre moments, P_N, the value of P_2/P_0 is found to be +56.4%. The hohlraum Z-axis is horizontal in this figure and in all figures in this paper.

III. MULTI-FLUID AND CROSSED-BEAM ENERGY TRANFER PHYSICS IN LASNEX

In the time following the publication of the work of Berzak Hopkins et al.,[43] two physics modules of interest were added to the radiation-hydrodynamic code LASNEX[52,53]. The most pertinent of these packages to the interpenetration hypothesis, was the addition of a 13-moment, multi-species package.

A. Multi-species physics

The multi-species (MS) model in LASNEX is based on the 13-moment model as described in the work of Schunk[55] (note that newer versions of LASNEX use a similar, but more numerically robust method[56]). The MS method divides the plasma into different "buckets", over which the 13 moment rate equations are solved individually. The buckets can correspond to different nuclides, can aggregate different nuclides, or can even be different instances of the same nuclide (e.g., carbon in the LEH window compared to carbon in the ablator). Each bucket has an individual velocity vector, temperature, and density (5-moments). Additionally, the 13-moment method means that each bucket has a stress tensor to allow for anisotropic pressure (5 more moments), and an ion heat flow vector (3 more moments). The anisotropic stress tensor models physical momentum diffusion, and thus physical viscosity is implicitly accounted for; however, numerical viscosity[57] is still included to accurately resolve shocks. The different buckets interact with each other through collisions[55,58], which set the exchange of momentum, temperature and higher moments.

The simulations shown in this paper have set the buckets corresponding to individual nuclides. Thus, a nuclide cannot interpenetrate with itself, for instance the carbon from the ablator will stagnate against carbon from the LEH window. We have run simulations where the ablator and LEH window carbon are put into different buckets, and this has not changed the results. Additionally, on-axis a bucket is not able to interpenetrate with itself due to the reflecting boundary, thus an individual bucket must stagnate on axis. Some of the anisotropy of this stagnation is captured through the anisotropic stress tensor, but it is not true interpenetration. In theory, we could include many buckets spaced across the spatial extent of the problem to include these effects. However, in practice, this becomes prohibitively computationally expensive.

B. Crossed-beam energy transfer physics

The other package of interest is the laser package. This uses standard geometric-optics ray-tracing[59], and assumes the laser light propagates infinitely fast. Inline models exist for laser plasma interactions including crossed-beam energy transfer (CBET), stimulated Raman scattering (SRS) and stimulated Brillouin scattering (SBS)[51]. Laser rays carry power, but the intensity of the other beams is needed for the LPI models. In this experiment, SRS and SBS are low and are not modeled here. CBET occurs when overlapping lasers beat to drive an ion acoustic wave, and this wave then transfers energy to the laser with the lower frequency in the plasma center-of-mass frame[60]. In many hohlraums, CBET is routinely used to transfer laser energy from outer to inner beams by optimizing the relative wavelength, $\Delta\lambda = \lambda_{\text{inner}} - \lambda_{\text{outer}}$, difference between the inner, λ_{inner}, and outer, λ_{outer}, laser wavelengths[61,62].

The evolution of the a laser a is governed by its vacuum frequency, ω_a, local electron density, n_e, and the critical density of the laser, $n_{\text{crit}} = \omega_a^2 \epsilon_0 m_e e^{-2}$, to set the local wavevector of the laser a, $\mathbf{k_a}$:

$$\mathbf{k_a} = \hat{\mathbf{k}}_\mathbf{a} (\omega_a / c) \sqrt{1 - n_e / n_{crit}}, \tag{1}$$

where $\hat{\mathbf{k}}_\mathbf{a}$ is the direction of the laser's wavevector. The laser ray direction is influenced through refraction in the plasma[59], $d\mathbf{v_g}/dt = -(c^2/2)\nabla(n_e/n_{crit})$, where $\mathbf{v_g}$ is the group velocity of the laser. The intensity, I_a, of the laser varies over its pathlength, z,

$$dI_a/dz = -\kappa I_a - \sum_{j \neq \alpha}^{N_b} g_c \, \omega_j^{-1} I_a I_j \tag{2}$$

where κ is the inverse Bremsstrahlung absorption coefficient. I_a is really a stand-in for the ray power, since all terms are linear in I_a. The CBET coupling is found under the assumptions typically made for rapid calculations in indirect-drive ICF: slow envelope variation (intensity and plasma gradients are small vs. the laser wavelength), the strong damping limit (Landau damping of the acoustic wave is strong enough that we can neglect its advection), the convective steady state, and linear-kinetic plasma-wave response. The CBET is calculated over all lasers, N_b being the number of lasers included in the simulation, which are grouped into 24 quads. The CBET coupling coefficient, g_c, between laser a and j is

$$g_c = G_0 k_{aj}^2 k_a^{-1} k_j^{-1} (1 + \cos^2\theta_{aj}) \, \mathrm{Im}(K) \tag{3}$$

where $G_0 = 2\epsilon_0 \pi^2 e^2 m_e^{-2} c^{-4}$ is a constant, $k_a = |\mathbf{k}_a|$ is the wavevector magnitude, θ_{aj} is the full-angle between the two lasers' k-vectors[51], and K is defined as:

$$K = \frac{\chi_e (1 + \sum \chi_i)}{1 + \chi_e + \sum \chi_i}. \tag{4}$$

The electron, $\chi_e(\mathbf{k}, \omega)$, and ion, $\chi_i(\mathbf{k}, \omega)$, susceptibilities

$$\chi_i(\mathbf{k}, \omega) = -\frac{1}{2k^2 \lambda_{Di}^2} Z' \left(\frac{\omega}{k v_{Ti}} \right) \tag{5}$$

are taken at $\mathbf{k} = \mathbf{k_{aj}} = \mathbf{k_a} - \mathbf{k_j}$, and $\omega = \omega_{aj} - \mathbf{k_{aj}} \cdot \mathbf{u}_i$, where $\omega_{aj} = \omega_a - \omega_j$ is the relative frequency and $\mathbf{u_i}$ is the velocity of the ions or electrons. The Debye length, λ_{Di}, is $\lambda_{Di}^2 = \epsilon_0 T_i/(n_i Z_i^2 e^2)$ and the thermal velocity, v_{Ti}, is $v_{Ti}^2 = 2T_i/m_i$. The susceptibility summation is taken over all ion buckets in the zone. This method assumes an isotropic, drifting Maxwellian for each ion bucket, and thus neglects the contribution of the anisotropic stress tensor and ion heat flow to CBET coupling.

The function $\mathrm{Im}(K)$ is maximized[63,64] when $\omega_{aj} - \mathbf{k_{aj}} \cdot \mathbf{u_i} = k_{aj} c_s$, where c_s is the sound speed. In the experiment of interest there is no applied shift of the laser wavelength, $\Delta\lambda = 0$, so $\omega_{aj} = 0$, and thus $\mathrm{Im}(K)$ is maximized when $\hat{\mathbf{k}}_{\mathbf{aj}} \cdot \mathbf{u}_i = c_s$. Thus, CBET is maximum when the wavevector difference of the lasers is aligned with a plasma flow traveling at the sound speed.

The inline CBET package utilizes a linear assumption for the power transfer between lasers. In this linear regime, we can calculate an amplitude of the electron density deviation of the ion acoustic wave, δn_e. For the linear assumption to be valid, $\delta n_e/n_e$ should be less than unity, and in any case it cannot be greater than unity. To include non-linear effects that will limit CBET as $\delta n_e/n_e$ approaches unity we include a "$\delta n_e/n_e$ cap" that will limit power transfer to the given wave amplitude.

IV. RESULTS FROM MULTI-SPECIES AND INLINE CBET SIMULATIONS

The simulations in this study use the LASNEX Hohlraum Template (LHT)[65]: a standardized, best-practices system to model hohlraums that has been developed over many iterations at LLNL. The LHT includes in the simulated geometry the external hardware used to mount the "window" that separates the hohlraum gas fill from the external vacuum. The window itself, the aluminum washer to which the window is attached, and the plastic retainer ring that holds the much thinner (∼100 nm) "storm window"[66] in place are all present and conformally meshed. The storm window material is not included. In order to match the "bangtime," associated with the peak x-ray emission from the capsule, we reduced the laser energy by 15% for all quads. All simulations shown in this paper utilize the 13-moment model[55]; we saw little difference between this and the 5-moment model. All simulations used an electron heat flux-limit[67] of 0.15. The simulations are one-sided along the Z-axis.

A. Single- and multi-species results without CBET

We begin by comparing the single-species (SS) and multi-species (MS) models in the case without CBET. The SS model without CBET is the closest to previous work, which used the code HYDRA[43]. The density of different ion species over time is shown in Fig. 4, where the ion density, n_i, times its ionization state, Z_i, is normalized by the critical density, n_{crit}. At early time, as seen in Fig. 4(a), the laser heats the region near the LEH window, which causes the carbon plasma to heat and push into the interior of the hohlraum. In the SS case, the carbon is not able to interpenetrate due to the single-species assumption, thus it cannot expand as far as in the MS case. Additionally, as shown in Fig. 4(b), in the SS case the carbon must expel all of the helium as it expands into the interior of the hohlraum. On the other hand, in the MS case interpenetration is possible given that the carbon and helium are allowed to have different velocities within a cell. This allows the carbon to expand further into the interior for the hohlraum, as shown in Fig. 4(a). As the carbon is able to interpenetrate through the helium gas in MS, the helium is not expelled from the region near to the LEH. At later times, we see this trend continue, where the carbon, Figs. 4(b-d), is able to expand further in the MS case. The difference between MS and SS is evident in the helium at later times, Figs. 4(g,h); in the SS case the helium is tightly restricted to the regions between carbon and helium expansion, but in the MS case the helium is nearly everywhere in the hohlraum.

Nonetheless, it is important to notice that the differences between the SS and MS cases occur mostly at low densities, $Z_i n_i/n_{\mathrm{crit}} < 0.01$, and thus despite the differences in appearance, we do not expect these lower densities to have much effect on the laser propagation. Additionally, as shown in Figs. 4(j-l), we find only minimal differences in the gold expansion between the two cases. We note that the overall similarity between the SS and MS simulations is not in agreement with the hypothesis proposed in the previous work[43], where it was theorized that the MS physics would dramatically alter the density in the hohlraum. As in the previous work[43], we find relative velocities of up to 600 km/s, which result in large interpenetration distances between ablated plasma from both the gold and carbon. However, due to the high densities of the ablated plasmas the interpenetration between gold and carbon is very similar in both SS and MS cases.

An additional difference between the simulations can be seen in the location of the aluminum plasma in Figs. 4(m-p). Given that the location of the aluminum is near the LEH, the density, velocity and temperature of the aluminum influence CBET. We note that this aluminum plasma is only present due to the inclusion of the hardware that holds the window in place; an important point that was shown in previous work[68]. The addition of this hardware is a relatively recent improvement to the LHT and would not have been included in most simulations prior to 2021.

To understand the laser propagation through the hohlraum, we plot the laser intensity and laser energy deposition during the laser peak power (∼6–7.5 ns) in Fig. 5. Similar to the previous work[43], we find that over time the lasers are not able to propagate all the way into the central waist of the hohlraum. This effect is not as pronounced at early times, Fig. 5(a), and is seen to increase dramatically by the end of the laser pulse,

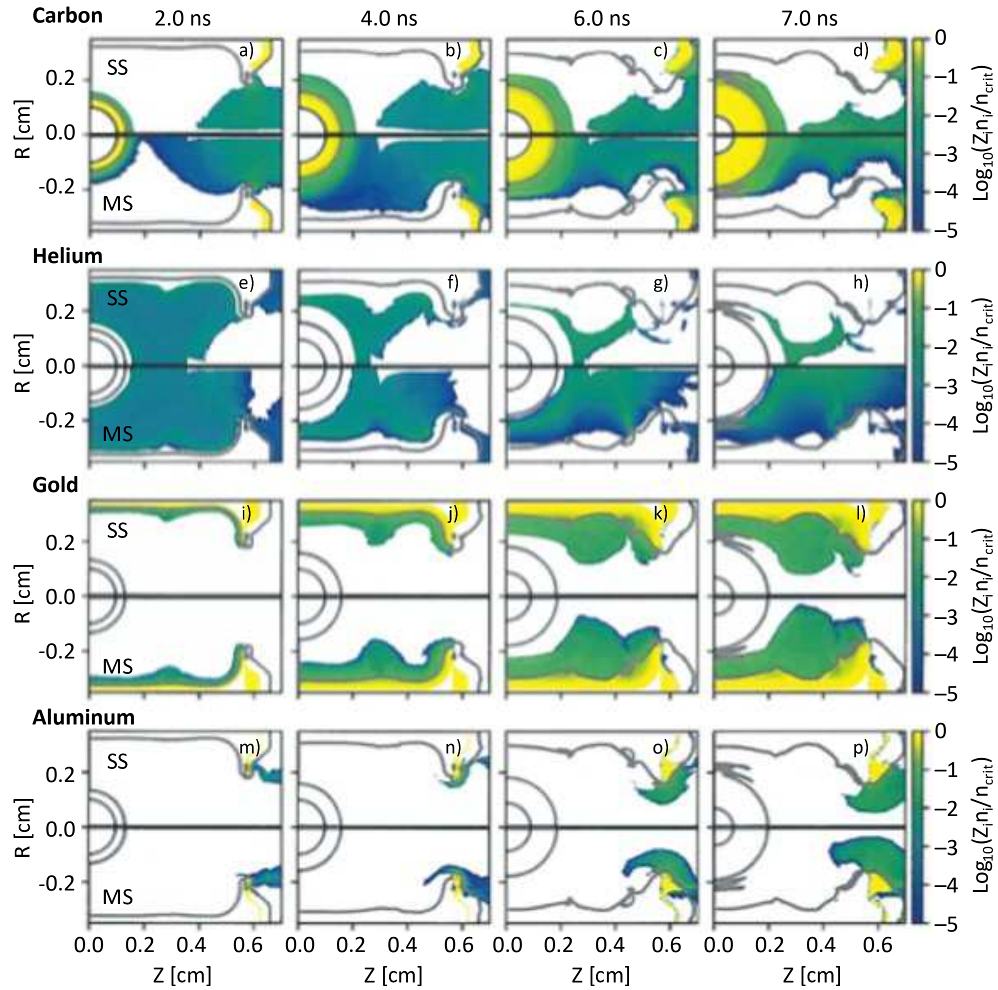

FIG. 4. Pseudocolor images of ion density, $Z_i n_i / n_{\mathrm{crit}}$. Carbon, helium, gold, and aluminum are show in the rows (a-d), (e-h). (i-l), and (m-p), respectively. The different times are indicated at the top of each column. The top and bottom of each subfigure show the SS and MS results, respectively. Gray curves indicate the contour where $n_e / n_{\mathrm{crit}} = 0.2$.

Fig. 5(d). However, again, unlike the expectation from previous work[43], we find that the laser propagation is nearly unchanged when including MS physics.

The capsule implosion is modeled in our simulation and the x-ray emission generated as the capsule heats and radiates. From this radiation, a time-integrated synthetic 2D image of the capsule x-ray emission is generated at the detector plane of the experimental diagnostic; the resulting x-ray images are show in Fig 6. In order to extract quantitative meaning, the image is fit with Legendre moments, P_N. As shown in Fig. 3, the experimental data is highly prolate ("sausage") with a P_2/P_0 moment of +56.4%. In contrast, both the SS and the MS simulations are highly oblate ("pancake"), with P_2/P_0 moments of −23.7% and −8.5%, respectively. Thus, while the MS physics causes P_2 to increase slightly, the values are still vastly different than the experimental data.

B. Multi-species results including CBET

To study the impact of crossed-beam energy transfer (CBET) on laser power and thus capsule implosion shape, we now look at a MS simulation with the inline CBET package activated. In this simulation, we use a "$\delta n_e / n_e$ cap" of 1%. From these simulations, we find that CBET does not make a major difference in the general evolution of the ion densities; the simulations look similar to Fig. 4.

To illustrate how CBET redistributes power from the outer to inner cones, we show the inner cone power divided by the total laser power in Fig. 7. The dashed curve is from the incident beams (pre-CBET) and the solid curve is post-CBET. Throughout peak power, > 4 ns, we see that the cone power fraction is dramatically increased by CBET, going from a peak of around 30% prior to CBET and up to 50% after CBET.

The powers of the individual cones are shown in Fig. 8, where again the dashed curve is pre-CBET and the solid

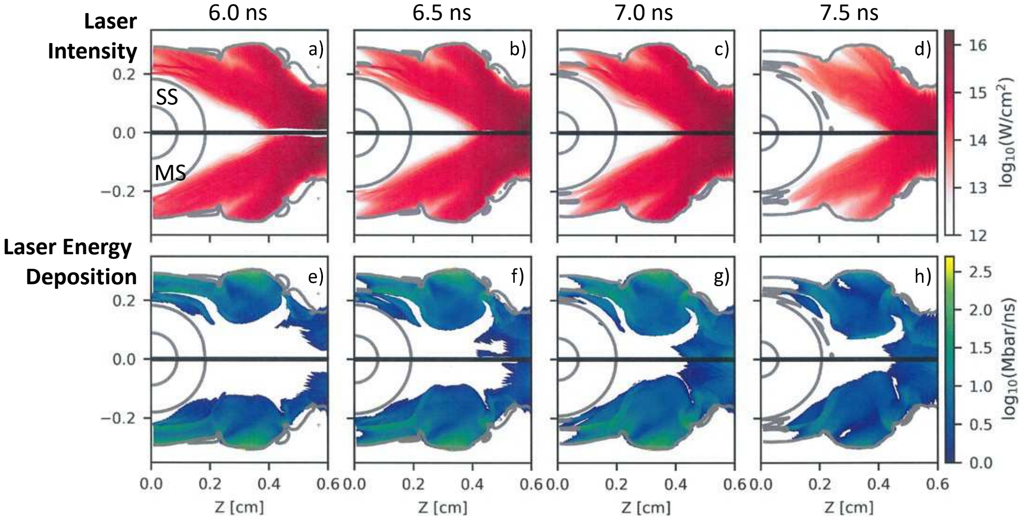

FIG. 5. Pseudocolor images of laser intensity (top row, a-d) and laser energy deposition per volume (bottom row, e-h) at different times during the laser peak power. The times are indicated at the top of each column. The top and bottom of each subfigure show the SS and MS results, respectively. Gray contours indicate the contour where $n_e/n_{\rm crit} = 0.2$.

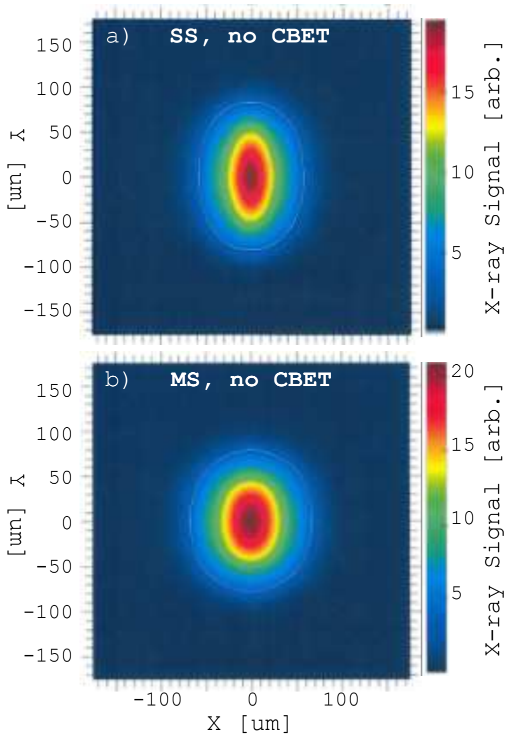

FIG. 6. Synthetic time-integrated capsule x-ray images for the a) SS and b) MS cases without CBET included. The P_2/P_0 moments are −23.7% for the SS and −8.5% for the MS case. The hohlraum Z-axis is horizontal in this figure, as in the previous figure.

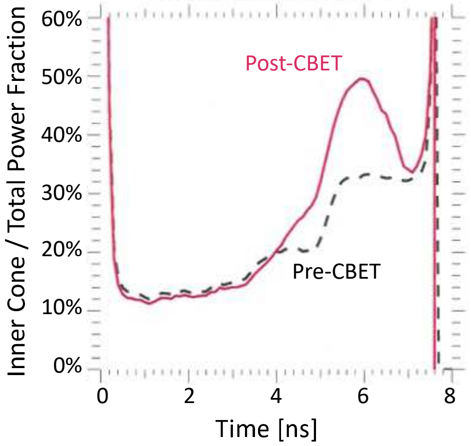

FIG. 7. Fraction of inner cone to total laser power in the MS + CBET simulation. Dashed and solid curves are pre- and post-CBET, respectively.

curve is post-CBET. Both inner cones, 23° and 30°, gain power with the inclusion of CBET, and the 44° outer cone loses energy over all times. However, the 50° outer cone loses energy at the start of beam power (up to 6 ns) and then gains power towards the end of the pulse. Recall that in this experiment there is no applied shift to the laser wavelengths, $\Delta\lambda = 0$, so all of the CBET is induced via flows traveling near the sound speed, and depends on the direction of the flow. Therefore the nature of the power transfer is highly dependent on the plasma conditions and thus, as we see from the 50° cone, the direction of power transfer can vary over time.

To better understand how CBET occurs, we plot the ion acoustic wave (IAW) power in Fig. 9(a-c) over three different times during peak laser power. The IAW power is a surrogate measurement of where the CBET is occurring spatially; the contour plotted on all panels of Fig. 9 indicates the region of highest IAW power.

In all of the times plotted, the maximum CBET occurs in the LEH at regions near to the axis, but not on the axis. As we see from the Fig. 9(d-f) the maximum of

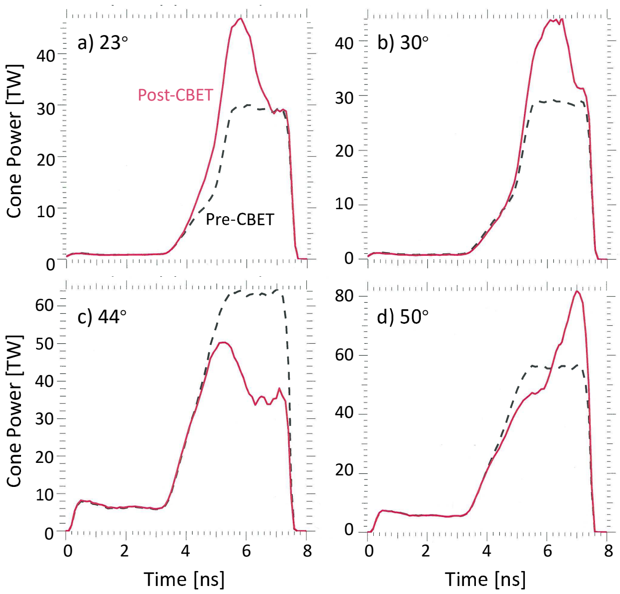

FIG. 8. Power of individual cones over time, where dashed and solid curves are pre- and post-CBET, respectively, in MS simulations.

the overlapped intensity always occurs on the laser axis. Thus, the maximum CBET is not occurring coincidently with the highest intensity. To better understand this phenomenon, we plot the radial velocity normalized to the sound speed, v_r/c_s, in Fig. 9(g-i). Given that there is no applied $\Delta\lambda$, the CBET coupling coefficient will be maximized when the plasma flow speed along $\hat{\mathbf{k}}_{\mathbf{aj}}$ is equal to the sound speed. Thus since $\hat{\mathbf{k}}_{\mathbf{aj}} \approx -\hat{\mathbf{r}}$, we expect the CBET coupling to be maximum where $v_r/c_s \simeq 1$. Thus from the plots of v_r/c_s in Fig. 9(g-i), we infer that CBET is not taking place on the axis because at this location the plasma flows have stagnated. Instead, CBET occurs slightly off-axis, where the plasma is flowing inwards. Of course, high laser intensity is required as well. For instance, in other regions, such as Fig. 9(g) at ($R = 0.1$ cm, $Z = 0.4$ cm) and ($R = 0.12$ cm, $Z = 0.6$ cm), there is little CBET due to the lack of overlap of the lasers even though in these regions $v_r/c_s \simeq 1$

As in the previous simulations, we create a synthetic x-ray emission image. The synthetic x-ray image for this simulation with MS physics and CBET ($\delta n_e/n_e$ cap of 1%) is shown in Fig 10. This image is fit with Legendre moments to attain values of $P_0 = 73.4$ μm and $P_2/P_0 = +53.1\%$. This image is now dramatically prolate. This is consistent with the experimental data, $P_2/P_0 = +56.4\%$, and is in stark contrast with the original SS simulations without CBET, which were dramatically oblate, $P_2/P_0 = -23.7\%$.

Thus we find that the inclusion of CBET makes a very impactful difference in the power distribution to the inner laser cones and the corresponding change in symmetry of the imploded capsule. Therefore, CBET is likely responsible for the highly prolate implosions observed experimentally.

C. Variation of the $\delta \mathbf{n_e}/\mathbf{n_e}$ cap, single-species CBET and the LEH hardware

One particular assumption that we make when using the inline CBET package is the value of the $\delta n_e/n_e$ cap. In the simulation shown above we used a cap of 1%, which is the "default" when using the LHT and in many hohlraum simulations. However, while this seems like a reasonable limit, the true physics governing the interaction when the wave amplitude becomes high are nonlinear and are not possible to include in LASNEX at this time. Instead, to understand the importance of this parameter, we scanned higher values of 2%, 5%, 10% and 20%. The resulting P_2/P_0 capsule symmetry of these simulations, including the results presented previously 0% (i.e., no CBET) and 1%, are shown in Fig. 11. In addition the the MS simulations (diamonds), the SS simulations (circles) and SS simulations without the inclusion of the external LEH hardware (crosses) are shown.

In general, at a certain value of the $\delta n_e/n_e$ cap the amount of P_2/P_0 capsule symmetry tends to saturate. In both the MS and SS cases, the symmetry saturates to a similar value, around 60%. However, the saturation occurs at lower cap in the MS simulations, around 1%, than in the SS simulations, around 5%. Nonetheless, for all of the caps other than 0%, we find that the simulations tend to highly prolate implosions. This shows that our conclusion that CBET influences capsule symmetry is robust.

Additionally, we show results from the simulations run without the addition of the LEH external hardware. This is an aluminum "washer" that holds in the thin window. In the past, this was thought to be a minor part of the hohlraum geometry and was therefore not included in the simulations. It was added to the LHT around the start of 2021. As shown by the crosses in Fig. 11, we find that the inclusion of the LEH hardware makes an important difference in the amount of CBET. In fact, without inclusion of the hardware, the maximum attainable P_2/P_0 capsule symmetry was around 25%. As was shown in Fig. 4(m-p), aluminum is a large component of the plasma in the area of the LEH, thus it is expected that including the hardware is important to capturing the physics of CBET accurately.

Fig. 12(a) shows the spatial locations of the ion species during peak power at 6 ns; the top panel includes the hardware in the simulation (HW), whereas the bottom panel does not (no-HW). In the HW simulation there is an additional region of aluminum, shown in red. This aluminum in the HW case has expanded more in the inner radial direction than the gold, shown in green, in the no-HW case due to the lower mass and thus higher sound speed of aluminum. As shown in Fig. 12(b), this aluminum causes the carbon in the LEH to expand towards axis at a faster velocity as well. The area over which the

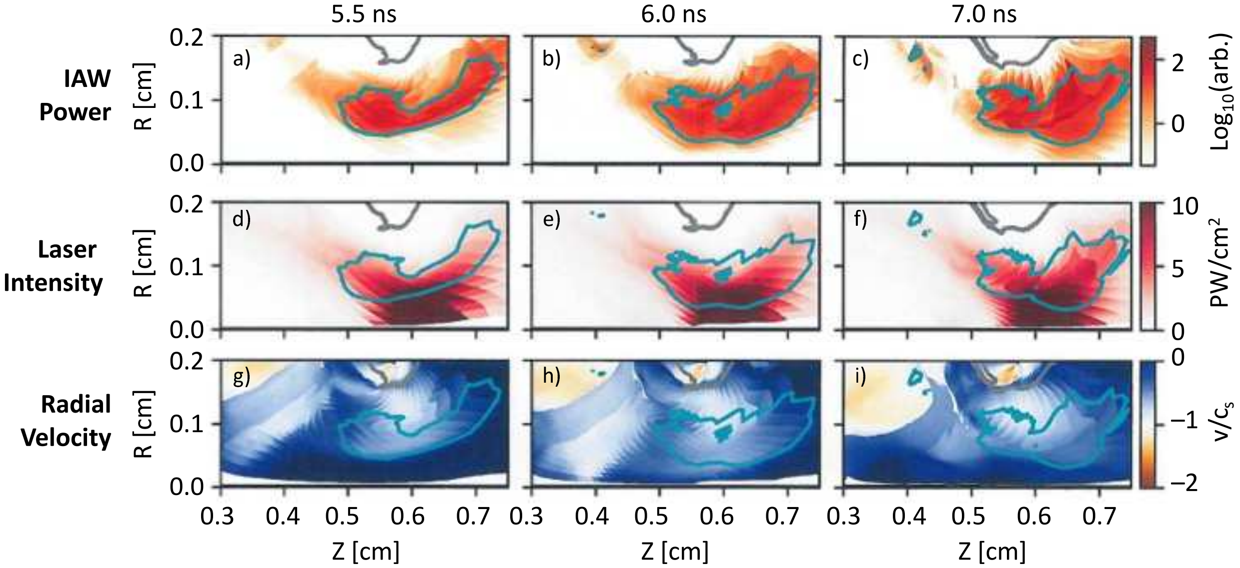

FIG. 9. Pseudocolor images of (a-c) ion acoustic wave (IAW) power, (d-f) laser intensity, and (g-i) radial plasma velocity normalized to the sound speed, for three different snapshots in time (5.5, 6.0, 7.0 ns) during peak power shown in different columns. The cyan contour curve plotted on all panels indicates the region of highest IAW power at that time. The gray contour indicates where $n_e/n_{\rm crit} = 0.2$; note that the LEH is around $Z = 0.6$ cm.

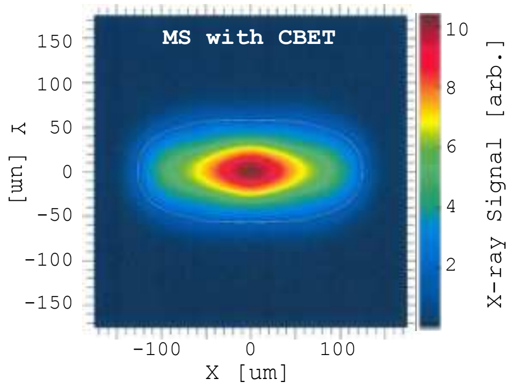

FIG. 10. Synthetic time-integrated capsule x-ray image of a simulation with MS physics and inline CBET included, the P_2/P_0 moment is +53.1%, which is close to the experimental data. The hohlraum Z-axis is horizontal in this figure, as in previous figures.

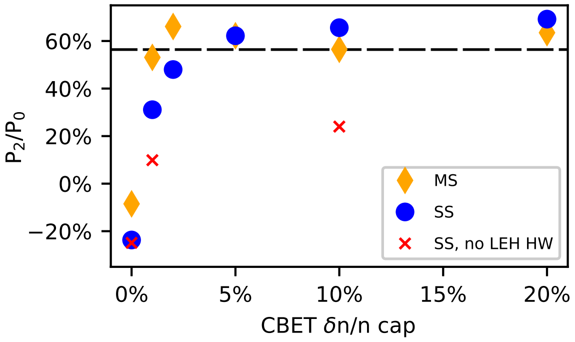

FIG. 11. P_2/P_0 capsule symmetry as a function of $\delta n_e/n_e$ cap for MS (diamonds), SS (circles) and SS without inclusion of the LEH external hardware (crosses). The dashed line indicates the experimental value of $P_2/P_0 = 56.4\%$.

carbon is moving faster corresponds to the region of highest laser intensity, as shown in Fig. 12(c), which causes CBET to be increased significantly in this region as inferred from the IAW power shown in Fig. 12(d). At this time of 6 ns, there is little CBET occuring in the aluminum itself, however, due to its faster expansion, the aluminum creates an environment that meets the CBET resonance condition, $v_r/c_s \simeq 1$, within the center of the LEH. Additionally, the faster expansion in the HW case causes higher electron density and hotter temperature on axis. We note that later in time, around 7 ns, the HW simulation shows CBET occurring in the aluminum plasma as well as the carbon.

We have not studied the differences between HYDRA and LASNEX in this work. However, we note that the previous work[43] using HYDRA did not include inline CBET or the LEH hardware at the time. Presently, HYDRA includes an inline CBET package including the same physics as LASNEX. In general, best practices evolve over time, and it would be take a significant amount of work to identify the exact differences and the impact of these differences between HYDRA in 2014/2015 and LASNEX in the present day. Nonetheless, we believe that investigating the experiment studied in our work with present day HYDRA would be a useful and informative study in the future.

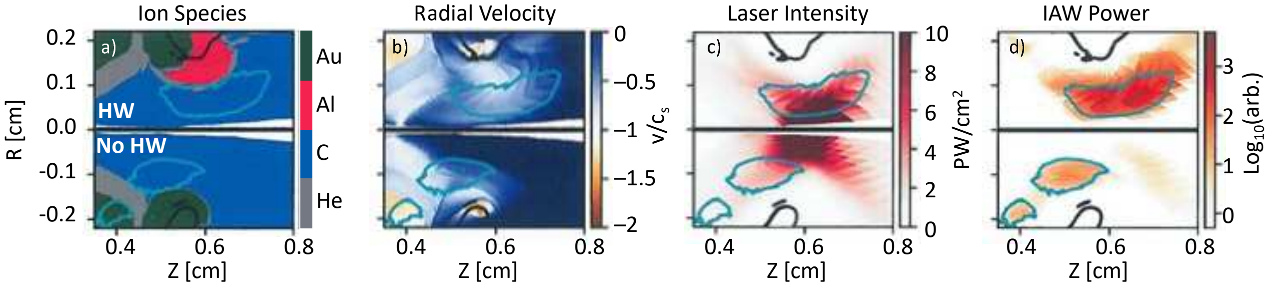

FIG. 12. Pseudocolor images of (a) ion species, (b) radial plasma velocity normalized to the sound speed, (c) laser intensity, and (d) ion acoustic wave (IAW) power, at 6 ns during peak power. The top panels are simulations including the LEH external hardware, while the bottom panels do not include the hardware. Both simulations are single-species and include inline CBET with a $\delta n_e/n_e$ cap of 1% . The cyan contour curve plotted on all panels indicates the region of highest IAW power at that time. The black contour indicates where $n_e/n_{\rm crit} = 0.2$; note that the LEH is around $Z = 0.6$ cm.

V. USE OF $\Delta\lambda$ TO ATTAIN CAPSULE SYMMETRY

Historically, the use of the near vacuum hohlraum (NVH) design, with a low fill density of 30 μg/cc, was abandoned given the lack of agreement between simulated and experimental P_2/P_0 capsule symmetry. Instead, the capsule fill density was increased to around 300 μg/cc to enter a regime where the simulations were more accurate[47]. However, to our knowledge, no simulations or experiments were attempted on this platform using an applied $\Delta\lambda$ to redistribute power from the inner to the outer beams and, thus, improve capsule implosion symmetry.

To investigate our ability to attain a symmetric capsule implosion in an NVH platform, we ran simulations with different amount of applied $\Delta\lambda$. The resulting P_2/P_0 capsule symmetry for different values of $\Delta\lambda = \lambda_{\rm inner} - \lambda_{\rm outer}$ at 1ω are shown in Fig. 13. Of particular interest is the ability to achieve a symmetric implosion using an applied $\Delta\lambda$ of -0.75 Å, which shows that it is possible to control the symmetry in such a way to make a viable experiment. NIF hohlraum experiments to date have had a positive $\Delta\lambda$, intended to increase inner beam power. However, the facility can deliver negative $\Delta\lambda$ as low as -1.0 Å at 1ω. The results also indicate that there is a mostly monotonic relationship between $\Delta\lambda$ and P_2/P_0 symmetry. However, we do find that the symmetry begins to plateau at a level of $\Delta\lambda$ above around $+0.5$ Å.

We plot the fraction of inner beam to total laser power for the different values of $\Delta\lambda$ in Fig. 14. As expected, higher values of $\Delta\lambda$ cause more energy to be transferred into the inner beams. Notice that at the highest value, $+1.2$ Å, the fraction is equivalent to or slightly lower than the $+0.6$ Å case, indicating a saturation of CBET. To illustrate the ability to perform symmetric implosions with the NVH platform, we show a synthetic capsule x-ray image with $\Delta\lambda$ of -0.75 Å in Fig. 15. This image shows excellent symmetry with a P_2/P_0 moment of only $+1.3\%$.

VI. IMPLICATIONS FOR NEAR VACUUM HOHLRAUMS

Historically, the (30 μg/cc) NVH platform was developed in the backdrop of much higher, 900 to 1600 μg/cc, hohlraum fill densities. These high fill densities used copious amounts of CBET to control P_2/P_0 capsule symmetry via $\Delta\lambda$, and had large amounts of SRS and SBS backscatter that reduced the efficiency of laser energy deposited in the hohlraum. The NVH was a complete change from this as there was negligible backscatter and CBET was not used to control symmetry – to date, no NIF shot with a hohlraum fill of ≤ 150 μg/cc has used a $\Delta\lambda$ between inner and outer beams.

The NVH experimental campaign occurred across a number of years and included: hohlraums with smaller diameters (D_H = 5.75 mm, and 6.20 mm) and capsule inner radii, R_{ic}, of 1 mm[44,69]; subscale hohlraums[70] (D_H = 5.75 mm, R_{ic} = 0.844 mm); and, larger hohlraums (D_H = 6.72 mm, R_{ic} = 1 mm)[43,45]. Over the course of these campaigns it was possible achieve capsule implosion symmetry through a combination of adjustments to the case-to-capsule ratio (CCR=$D_H/(2R_{ic})$), the laser pulse duration, and the ratio of power into inner and outer beams. Radiation-hydrodynamic simulations were able to match the experimental data, but only by using an *ad hoc* modification to the laser wavelength. This "enhanced propagation model" changed the frequency of the inner beams from the nominal 3ω, often to 4ω or 5ω, though up to a maximum of 9ω, and, at times, reduced the outer beam frequency to 2ω. The physical justification for this modification was that the single-fluid codes did not accurately model interpenetration and diffusion, and thus over-predicted the electron density and artificially obstructed inner beam propagation. This hypothesis is what initially motivated our simulations using the multi-species (MS) model in LASNEX, however we did not find this to substantially change capsule symmetry. Instead we found that CBET played a major role in modifying the fraction of energy into inner and outer beams. Unlike the previous model, we did not use *ad hoc* multipliers on the beam wavelength to control symmetry;

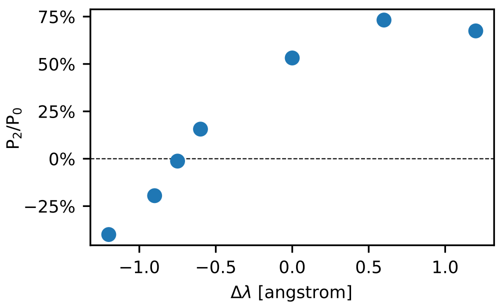

FIG. 13. Control of P_2/P_0 capsule symmetry by applied $\Delta\lambda = \lambda_{\rm inner} - \lambda_{\rm outer}$ at 1ω. Here the $\delta n_e/n_e$ cap is 1%.

instead, we used improvements in the physics modules of the codes that are now in general usage. This allowed us to draw conclusions related to the physics and apply these to optimize the implosion symmetry.

The ability to control capsule symmetry and achieve a symmetric implosion via simulation is encouraging. It implies a sufficient understanding of the physics of using 30 μg/cc fills to make experimental designs feasible with our current simulation capabilities. Of course, there may be other drawbacks to using these low fills, such as reduced tamping of the expansion of the hohlraum walls (e.g., the gold "bubble") that may require a shorter laser pulse duration or larger case-to-capsule ratio[71]. Additionally, the inner cone power fraction in Fig. 14 shows significant swings when CBET is taken into account even when applying a $\Delta\lambda$ of -0.75 Å that results in a symmetric implosion. By extracting the ablation pressure from the simulation and decomposing it into Legendre moments, we find variations in P_2/P_0 drive of $\pm 5\%$ during peak power. Such swings have been shown to degrade performance even when the capsule achieves symmetry at stagnation[72] and thus should be reduced for a more robust experimental design. As with any ICF experimental platform, the design must be optimized considering many different aspects, of which hohlraum gas fill is only one. Nonetheless, by achieving an understanding of the physics at these lowest gas fills, we believe that these lowest fills are no longer "off-limits" in terms of hohlraum design considerations.

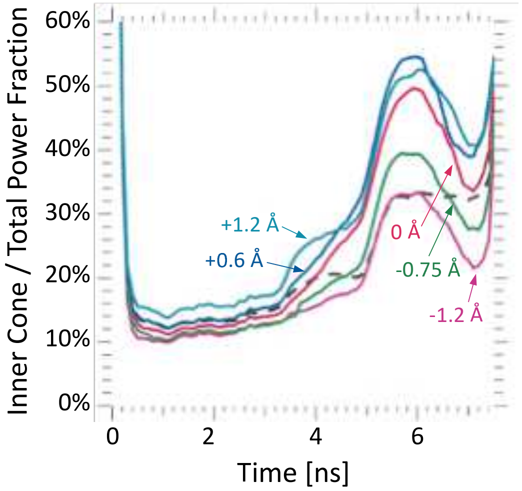

FIG. 14. Fraction of inner cone to total laser power, for different values of applied Δλ as indicated on the plot. The dashed curve indicates the incident pre-CBET values. Here the $\delta n_e/n_e$ cap is 1%.

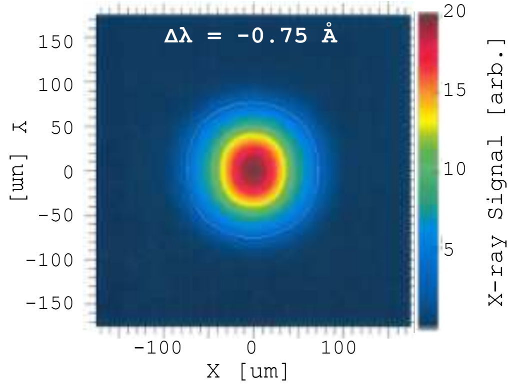

FIG. 15. Synthetic time-integrated capsule x-ray image of a simulation with an applied $\Delta\lambda$ of -0.75 Å. MS physics and inline CBET are included. The P_2/P_0 moment is +1.3%. The hohlraum Z-axis is horizontal in this figure, as in the previous figure.

VII. SUMMARY

We presented some of the first physics results modeling hohlraums using the multi-species package in the radiation-hydrodynamic code LASNEX. Our investigation focused on the near vacuum hohlraum (NVH) design, shot N140702-001, with a low fill density of 30 μg/cc. As this is the lowest fill density used on the National Ignition Facility, it is the most likely situation for strong multi-species physics effects, such as interpenetration, to be present. Additionally, there has been a long standing enigma of P_2/P_0 capsule symmetry in this design; the code predicted highly oblate implosions while experiments showed highly prolate implosions. However, even at these low densities our investigations found that the use of MS physics alone was not enough to shift the capsule symmetry from oblate to prolate. Instead, the application of inline cross-beam energy transfer (CBET), with the important addition of the hohlraum laser entrance hole (LEH) hardware, was found to transfer large amounts of laser power from the outer to inner lasers. This modified power profile caused the P_2/P_0 capsule symmetry to become strongly prolate in the simulations, which is in agreement with the experimental data. This is evidence that the longstanding symmetry enigma in the NVH was caused by CBET instead of multi-species physics, and gives us confidence that even these lowest densities can be modeled accurately using hydrodynamics simulations.

With this knowledge of the importance of CBET, we showed that it is theoretically possible to create symmetric implosions by applying a negative wavelength shift between the inner and outer beams, $\Delta\lambda = \lambda_{\text{inner}} - \lambda_{\text{outer}}$, of -0.75 Å at 1ω to transfer power from the inner to outer beams (unlike the positive $\Delta\lambda$ used so far on NIF hohlraums). These results show that the NVH is potentially a viable ICF platform. Historically, the ICF program has achieved impressive gains when moving from higher (1.6 mg/cc) to lower (600 μg/cc) gas fills[46]. Experimental evidence[48] shows a additional 10% increase in laser-to-drive efficiency going from 600 to 30 μg/cc; thus making it likely that there are additional gains to be obtained. More efficient hohlraums could allow for larger case-to-capsule ratios, and thus improvements in implosion stability, or could simply put more energy into the drive to create faster and hotter implosions. Given our success in understanding and modeling this platform through improvements to the physics of the simulations, we believe the use the the lowest, 30 μg/cc, hohlraum fill can serve as a useful tool on the pathway to inertial confinement fusion.

ACKNOWLEDGMENTS

Thanks to Laurent Divol, Denise Hinkel, Will Riedel, Mordy Rosen, Steven Ross, and Oggie Jones for useful comments and discussion. This work was performed under the auspices of the U.S. Department of Energy by Lawrence Livermore National Laboratory (LLNL) under Contract DE-AC52-07NA27344. This document was prepared as an account of work sponsored by an agency of the United States government. Neither the United States government nor Lawrence Livermore National Security, LLC, nor any of their employees makes any warranty, expressed or implied, or assumes any legal liability or responsibility for the accuracy, completeness, or usefulness of any information, apparatus, product, or process disclosed, or represents that its use would not infringe privately owned rights. Reference herein to any specific commercial product, process, or service by trade name, trademark, manufacturer, or otherwise does not necessarily constitute or imply its endorsement, recommendation, or favoring by the United States government or Lawrence Livermore National Security, LLC. The views and opinions of authors expressed herein do not necessarily state or reflect those of the United States government or Lawrence Livermore National Security, LLC, and shall not be used for advertising or product endorsement purposes. The data that support the findings of this study are available from the corresponding author upon reasonable request.

[37] J. D. Lindl, P. Amendt, R. L. Berger, S. G. Glendinning, S. H. Glenzer, S. W. Haan, R. L. Kauffman, O. L. Landen, and L. J. Suter, Physics of plasmas **11**, 339 (2004).

[38] Atzeni and Meyer-Ter-Vehn, *The Physics of Inertial Fusion* (Oxford Univesity Press, 2004).

[39] G. Kyrala, J. Kline, S. Dixit, S. Glenzer, D. Kalantar, D. Bradley, N. Izumi, N. Meezan, O. Landen, D. Callahan, et al., Physics of Plasmas **18**, 056307 (2011).

[40] J. L. Kline, D. A. Callahan, S. H. Glenzer, N. B. Meezan, J. D. Moody, D. E. Hinkel, O. S. Jones, A. J. MacKinnon, R. Bennedetti, R. L. Berger, et al., Physics of Plasmas **20**, 056314 (2013).

[41] O. A. Hurricane, D. A. Callahan, D. T. Casey, E. L. Dewald, T. R. Dittrich, T. Döppner, S. Haan, D. E. Hinkel, L. F. Berzak Hopkins, O. Jones, et al., Nature Physics **12**, 800 (2016).

[42] E. I. Moses, R. N. Boyd, B. A. Remington, C. J. Keane, and R. Al-Ayat, Physics of Plasmas **16**, 041006 (2009).

[43] L. Berzak Hopkins, S. Le Pape, L. Divol, N. Meezan, A. Mackinnon, D. Ho, O. Jones, S. Khan, J. Milovich, J. Ross, et al., Phys. Plasmas **22**, 056318 (2015).

[44] L. Berzak Hopkins, N. Meezan, S. Le Pape, L. Divol, A. Mackinnon, D. Ho, M. Hohenberger, O. Jones, G. Kyrala, J. Milovich, et al., Phys. Rev. Lett. **114**, 175001 (2015).

[45] S. Le Pape, L. F. Berzak Hopkins, L. Divol, N. Meezan, D. Turnbull, A. J. Mackinnon, D. Ho, J. S. Ross, S. Khan, A. Pak, et al., Physics of Plasmas **23**, 056311 (2016).

[46] D. E. Hinkel, L. F. Berzak Hopkins, T. Ma, J. E. Ralph, F. Albert, L. R. Benedetti, P. M. Celliers, T. Döppner, C. S. Goyon, N. Izumi, et al., Physical review letters **117**, 225002 (2016).

[47] L. Divol, A. Pak, L. Berzak Hopkins, S. L. Pape, N. Meezan, E. Dewald, D.-M. Ho, S. Khan, A. Mackinnon, J. Ross, et al., Phys. Plasma **24**, 056309 (2017).

[48] G. N. Hall, O. S. Jones, D. J. Strozzi, J. D. Moody, D. Turnbull, J. Ralph, P. A. Michel, M. Hohenberger, A. S. Moore, O. L. Landen, et al., Physics of Plasmas **24**, 052706 (2017).

[49] S. Le Pape, L. Divol, G. Huser, J. Katz, A. Kemp, J. S. Ross, R. Wallace, and S. Wilks, Physical review letters **124**, 025003 (2020).

[50] D. P. Higginson, P. Amendt, N. Meezan, W. Riedel, H. G. Rinderknecht, S. C. Wilks, and G. Zimmerman, Phys. Plasmas **26**, 112107 (2019).

[51] D. J. Strozzi, D. S. Bailey, P. Michel, L. Divol, S. M. Sepke, G. D. Kerbel, C. A. Thomas, J. E. Ralph, J. D. Moody, and M. B. Schneider, Physical review letters **118**, 025002 (2017).

[52] G. B. Zimmerman and W. L. Kruer, Comments Plasma Phys. Controlled Fusion **2**, 51 (1975).

[53] J. A. Harte, W. E. Alley, D. S. Bailey, J. L. Eddleman, and G. B. Zimmerman (1996).

[54] M. M. Marinak, G. D. Kerbel, N. A. Gentile, O. Jones, D. Munro, S. Pollaine, T. R. Dittrich, and S. W. Haan, Phys. Plasmas **8**, 2275 (2001).

[55] R. W. Schunk, Reviews of Geophysics **15**, 429 (1977).

[56] S. T. Miller and U. Shumlak, Physics of Plasmas **23**, 082303 (2016).

[57] J. VonNeumann and R. D. Richtmyer, Journal of applied physics **21**, 232 (1950).

[58] L. G. Stanton and M. S. Murillo, Physical Review E **93**, 043203 (2016).

[59] T. B. Kaiser, Physical Review E **61**, 895 (2000).

[60] W. L. Kruer, S. C. Wilks, B. B. Afeyan, and R. K. Kirkwood, Physics of Plasmas **3**, 382 (1996).

[61] P. Michel, L. Divol, E. A. Williams, S. Weber, C. A. Thomas, D. A. Callahan, S. W. Haan, J. D. Salmonson, S. Dixit, D. E. Hinkel, et al., Physical review letters **102**, 025004 (2009).

[62] P. Michel, S. Glenzer, L. Divol, D. Bradley, D. Callahan, S. Dixit, S. Glenn, D. Hinkel, R. Kirkwood, J. Kline, et al., Physics of Plasmas **17**, 056305 (2010).

[63] C. J. Randall, J. R. Albritton, and J. J. Thomson, The Physics of Fluids **24**, 1474 (1981).

[64] J. W. Bates, R. K. Follett, J. G. Shaw, S. P. Obenschain, R. H. Lehmberg, J. F. Myatt, J. L. Weaver, D. M. Kehne, M. F. Wolford, M. C. Myers, et al., High Energy Density Physics **36**, 100772 (2020).

[65] O. S. Jones, L. J. Suter, H. A. Scott, M. A. Barrios, W. A. Farmer, S. B. Hansen, D. A. Liedahl, C. W. Mauche, A. S. Moore,

M. D. Rosen, et al., Phys. Plasmas **24**, 056312 (2017).

[66] H. F. Robey, T. R. Boehly, P. M. Celliers, J. H. Eggert, D. Hicks, R. F. Smith, R. Collins, M. W. Bowers, K. G. Krauter, P. S. Datte, et al., Physics of Plasmas **19**, 042706 (2012).

[67] M. D. Rosen, H. A. Scott, D. E. Hinkel, E. A. Williams, D. A. Callahan, R. P. J. Town, L. Divol, P. A. Michel, W. L. Kruer, L. J. Suter, et al., High Energy Density Physics **7**, 180 (2011).

[68] P. Amendt, D. Ho, Y. Ping, V. Smalyuk, S. Khan, J. Lindl, D. Strozzi, R. Tommasini, M. Belyaev, C. Cerjan, et al., Physics of Plasmas **26**, 082707 (2019).

[69] N. B. Meezan, L. F. Berzak Hopkins, S. Le Pape, L. Divol, A. J. MacKinnon, T. Döppner, D. D. Ho, O. S. Jones, S. F. Khan, T. Ma, et al., Physics of Plasmas **22**, 062703 (2015).

[70] D. Turnbull, L. Berzak Hopkins, S. Le Pape, L. Divol, N. Meezan, O. L. Landen, D. D. Ho, A. Mackinnon, A. B. Zylstra, H. G. Rinderknecht, et al., Physics of Plasmas **23**, 052710 (2016).

[71] D. A. Callahan, O. A. Hurricane, J. E. Ralph, C. A. Thomas, K. L. Baker, L. R. Benedetti, L. F. Berzak Hopkins, D. T. Casey, T. Chapman, C. E. Czajka, et al., Physics of Plasmas **25**, 056305 (2018).

[72] A. L. Kritcher, R. Town, D. Bradley, D. Clark, B. Spears, O. Jones, S. Haan, P. T. Springer, J. Lindl, R. H. H. Scott, et al., Physics of Plasmas **21**, 042708 (2014).

[37] J. D. Lindl, P. Amendt, R. L. Berger, S. G. Glendinning, S. H. Glenzer, S. W. Haan, R. L. Kauffman, O. L. Landen, and L. J. Suter, Physics of plasmas **11**, 339 (2004).

[38] Atzeni and Meyer-Ter-Vehn, *The Physics of Inertial Fusion* (Oxford Univesity Press, 2004).

[39] G. Kyrala, J. Kline, S. Dixit, S. Glenzer, D. Kalantar, D. Bradley, N. Izumi, N. Meezan, O. Landen, D. Callahan, et al., Physics of Plasmas **18**, 056307 (2011).

[40] J. L. Kline, D. A. Callahan, S. H. Glenzer, N. B. Meezan, J. D. Moody, D. E. Hinkel, O. S. Jones, A. J. MacKinnon, R. Bennedetti, R. L. Berger, et al., Physics of Plasmas **20**, 056314 (2013).

[41] O. A. Hurricane, D. A. Callahan, D. T. Casey, E. L. Dewald, T. R. Dittrich, T. Döppner, S. Haan, D. E. Hinkel, L. F. Berzak Hopkins, O. Jones, et al., Nature Physics **12**, 800 (2016).

[42] E. I. Moses, R. N. Boyd, B. A. Remington, C. J. Keane, and R. Al-Ayat, Physics of Plasmas **16**, 041006 (2009).

[43] L. Berzak Hopkins, S. Le Pape, L. Divol, N. Meezan, A. Mackinnon, D. Ho, O. Jones, S. Khan, J. Milovich, J. Ross, et al., Phys. Plasmas **22**, 056318 (2015).

[44] L. Berzak Hopkins, N. Meezan, S. Le Pape, L. Divol, A. Mackinnon, D. Ho, M. Hohenberger, O. Jones, G. Kyrala, J. Milovich, et al., Phys. Rev. Lett. **114**, 175001 (2015).

[45] S. Le Pape, L. F. Berzak Hopkins, L. Divol, N. Meezan, D. Turnbull, A. J. Mackinnon, D. Ho, J. S. Ross, S. Khan, A. Pak, et al., Physics of Plasmas **23**, 056311 (2016).

[46] D. E. Hinkel, L. F. Berzak Hopkins, T. Ma, J. E. Ralph, F. Albert, L. R. Benedetti, P. M. Celliers, T. Döppner, C. S. Goyon, N. Izumi, et al., Physical review letters **117**, 225002 (2016).

[47] L. Divol, A. Pak, L. Berzak Hopkins, S. L. Pape, N. Meezan, E. Dewald, D.-M. Ho, S. Khan, A. Mackinnon, J. Ross, et al., Phys. Plasma **24**, 056309 (2017).

[48] G. N. Hall, O. S. Jones, D. J. Strozzi, J. D. Moody, D. Turnbull, J. Ralph, P. A. Michel, M. Hohenberger, A. S. Moore, O. L. Landen, et al., Physics of Plasmas **24**, 052706 (2017).

[49] S. Le Pape, L. Divol, G. Huser, J. Katz, A. Kemp, J. S. Ross, R. Wallace, and S. Wilks, Physical review letters **124**, 025003 (2020).

[50] D. P. Higginson, P. Amendt, N. Meezan, W. Riedel, H. G. Rinderknecht, S. C. Wilks, and G. Zimmerman, Phys. Plasmas **26**, 112107 (2019).

[51] D. J. Strozzi, D. S. Bailey, P. Michel, L. Divol, S. M. Sepke, G. D. Kerbel, C. A. Thomas, J. E. Ralph, J. D. Moody, and M. B. Schneider, Physical review letters **118**, 025002 (2017).

[52] G. B. Zimmerman and W. L. Kruer, Comments Plasma Phys. Controlled Fusion **2**, 51 (1975).

[53] J. A. Harte, W. E. Alley, D. S. Bailey, J. L. Eddleman, and G. B. Zimmerman (1996).

[54] M. M. Marinak, G. D. Kerbel, N. A. Gentile, O. Jones, D. Munro, S. Pollaine, T. R. Dittrich, and S. W. Haan, Phys. Plasmas **8**, 2275 (2001).

[55] R. W. Schunk, Reviews of Geophysics **15**, 429 (1977).

[56] S. T. Miller and U. Shumlak, Physics of Plasmas **23**, 082303 (2016).

[57] J. VonNeumann and R. D. Richtmyer, Journal of applied physics **21**, 232 (1950).

[58] L. G. Stanton and M. S. Murillo, Physical Review E **93**, 043203 (2016).

[59] T. B. Kaiser, Physical Review E **61**, 895 (2000).

[60] W. L. Kruer, S. C. Wilks, B. B. Afeyan, and R. K. Kirkwood, Physics of Plasmas **3**, 382 (1996).

[61] P. Michel, L. Divol, E. A. Williams, S. Weber, C. A. Thomas, D. A. Callahan, S. W. Haan, J. D. Salmonson, S. Dixit, D. E. Hinkel, et al., Physical review letters **102**, 025004 (2009).

[62] P. Michel, S. Glenzer, L. Divol, D. Bradley, D. Callahan, S. Dixit, S. Glenn, D. Hinkel, R. Kirkwood, J. Kline, et al., Physics of Plasmas **17**, 056305 (2010).

[63] C. J. Randall, J. R. Albritton, and J. J. Thomson, The Physics of Fluids **24**, 1474 (1981).

[64] J. W. Bates, R. K. Follett, J. G. Shaw, S. P. Obenschain, R. H. Lehmberg, J. F. Myatt, J. L. Weaver, D. M. Kehne, M. F. Wolford, M. C. Myers, et al., High Energy Density Physics **36**, 100772 (2020).

[65] O. S. Jones, L. J. Suter, H. A. Scott, M. A. Barrios, W. A. Farmer, S. B. Hansen, D. A. Liedahl, C. W. Mauche, A. S. Moore, M. D. Rosen, et al., Phys. Plasmas **24**, 056312 (2017).

[66] H. F. Robey, T. R. Boehly, P. M. Celliers, J. H. Eggert, D. Hicks, R. F. Smith, R. Collins, M. W. Bowers, K. G. Krauter, P. S. Datte, et al., Physics of Plasmas **19**, 042706 (2012).

[67] M. D. Rosen, H. A. Scott, D. E. Hinkel, E. A. Williams, D. A. Callahan, R. P. J. Town, L. Divol, P. A. Michel, W. L. Kruer, L. J. Suter, et al., High Energy Density Physics **7**, 180 (2011).

[68] P. Amendt, D. Ho, Y. Ping, V. Smalyuk, S. Khan, J. Lindl, D. Strozzi, R. Tommasini, M. Belyaev, C. Cerjan, et al., Physics of Plasmas **26**, 082707 (2019).

[69] N. B. Meezan, L. F. Berzak Hopkins, S. Le Pape, L. Divol, A. J. MacKinnon, T. Döppner, D. D. Ho, O. S. Jones, S. F. Khan, T. Ma, et al., Physics of Plasmas **22**, 062703 (2015).

[70] D. Turnbull, L. Berzak Hopkins, S. Le Pape, L. Divol, N. Meezan, O. L. Landen, D. D. Ho, A. Mackinnon, A. B. Zylstra, H. G. Rinderknecht, et al., Physics of Plasmas **23**, 052710 (2016).

[71] D. A. Callahan, O. A. Hurricane, J. E. Ralph, C. A. Thomas, K. L. Baker, L. R. Benedetti, L. F. Berzak Hopkins, D. T. Casey, T. Chapman, C. E. Czajka, et al., Physics of Plasmas **25**, 056305 (2018).

[72] A. L. Kritcher, R. Town, D. Bradley, D. Clark, B. Spears, O. Jones, S. Haan, P. T. Springer, J. Lindl, R. H. H. Scott, et al., Physics of Plasmas **21**, 042708 (2014).